

## Use of RTM full 3D subsurface angle gathers for subsalt velocity update and image optimization: Case study at Shenzi field

Zheng-Zheng Zhou<sup>1</sup>, Michael Howard<sup>2</sup>, and Cheryl Mifflin<sup>2</sup>

### ABSTRACT

Various reverse time migration (RTM) angle gather generation techniques have been developed to address poor subsalt data quality and multiarrival induced problems in gathers from Kirchhoff migration. But these techniques introduce new problems, such as inaccuracies in 2D subsurface angle gathers and edge diffraction artifacts in 3D subsurface angle gathers. The unique rich-azimuth data set acquired over the Shenzi field in the Gulf of Mexico enabled the generally artifact-free generation of 3D subsurface angle gathers. Using this data set, we carried out suprasalt tomography and salt model building steps and then produced 3D angle gathers to update the subsalt velocity. We used tilted transverse isotropy RTM with extended image condition to generate full 3D subsurface offset domain common image gathers, which were subsequently converted to 3D angle gathers. The angle gathers were substacked along the subsurface azimuth axis into azimuth sectors. Residual moveout analysis was carried out, and ray-based tomography was used to update velocities. The updated velocity model resulted in improved imaging of the subsalt section. We also applied residual moveout and selective stacking to 3D angle gathers from the final migration to produce an optimized stack image.

### INTRODUCTION

The data was acquired with rich-azimuth towed streamer geometry (Howard, 2007). It consists of three subdata sets, each comprising a three-tile wide-azimuth data set in its own right. The three subdata sets were shot at, respectively, 30°, 90°, and 150° of azimuth counterclockwise from north. The resulting survey has nearly uniform surface azimuth coverage (Figure 1). This

geometry enhanced our ability to better remove multiples through multiazimuth 3D surface related multiple elimination (SRME) and our ability to obtain a good suprasalt sediment velocity model through multiazimuth tilted transverse isotropy (TTI) tomography.

One crucial advantage of full azimuth coverage is the removal of artifacts from reverse time migration (RTM) 3D subsurface angle gathers. Tomographical migration velocity updates requires common image gathers (CIGs). In the context of subsalt velocity update, conventional CIGs produced by Kirchhoff migrations suffer from low data quality and multipathing induced artifacts (Nolan and Symes, 1996; Xu et al., 2001). Methods for producing subsurface angle gathers from non-ray-based migrations have been introduced to solve these problems. Shot profile, delayed shot, plane-wave shot, and phase encoded shot migrations, etc., are the class of migrations that use some type of wave equation to separately propagate a source-generated incident wavefield and a scattered wavefield and use an imaging condition at each subsurface point to form the image from these two wavefields. Most RTM and wave equation migration (WEM) implementations fall into this category. Subsurface angle gathers can be generated from such migrations through a variety of techniques, depending on whether decomposition is performed on the wavefields or performed in the image domain. These techniques include 1) those involving plane-wave decomposition of the wavefields prior to application of imaging condition (Soubaras, 2003; Wu et al., 2004; Xu et al., 2010), 2) those involving polarization analysis of the wavefields prior to imaging condition (Yoon et al., 2004; Macesanu et al., 2010), and 3) those employing extended imaging conditions (de Bruin et al., 1990; Sava and Vasconcelos, 2011) to generate subsurface offset and/or time-shift gathers that are converted to angle gathers after migration.

In the third category, there are a variety of extended images that can be converted into angle gathers, including 3a) time-shift gathers (Sava and Fomel, 2006), 3b) subsurface inline-offset gathers (Rickett and Sava, 2002), 3c) subsurface offset-vector gathers (Biondi and Tisserant, 2004; Fomel, 2004), and 3d) higher-dimensional extended

Manuscript received by the Editor 14 February 2011; revised manuscript received 6 May 2011; published online 21 November 2011.

<sup>1</sup>ION Geophysical, GXT Imaging, Houston, Texas, USA. E-mail: zzz@gxt.com.

<sup>2</sup>BHP Billiton, Houston, Texas, USA. E-mail: Mike.Howard@BHPBilliton.com; Cheryl.Mifflin@bhpbilliton.com.

© 2011 Society of Exploration Geophysicists. All rights reserved.

images which currently are not commonly used in practice for angle gathers due to very high cost. Method 3a can generate angle gathers for both 2D and 3D situations, but it does not preserve any azimuthal information. It also has very low angular resolution for incidence angles below  $20^\circ$ , a result of the angle mapping's reliance on the cosine to distinguish between angles. The mapping is based on the observation that the relation between time shift and depth shift contains a cosine of the incidence angle. In contrast, method 3b has good angular resolution for low angles of incidence because it uses the tangent to distinguish between angles. In Figure 2, we compare gathers from these two methods. Here, the input synthetic data was migrated with a velocity model that is uniformly too fast by 4%. The low angular resolution of method 3a causes traces within  $15^\circ$  to be largely identical. As a result, the residual moveout is distorted and appears to lack a quadratic term. Note that the available maximum angle subsalt is less than  $20^\circ$  in many situations. The gather from method 3b does not have this problem and displays the approximately hyperbolic moveout expected under this test.

While it has good angle resolution, method 3b is limited by its assumption of 2D wave propagation and maps energy incorrectly in 3D situations. For instance, in a 3D case where the reflector has zero crossline dip but the reflection plane (the plane formed by the incident and reflected ray vectors) has nonzero azimuth, the 2D angle mapping will underestimate the angle of incidence. And conversely, in the situation of zero reflection-plane azimuth, this mapping will overestimate the angle when the reflector has crossline dip. These errors of the 2D angle mapping can be derived from equation 16 in Fomel (2004), and are discussed in Biondi (2006). In general, the 2D approximation is ill-suited for full-azimuth data.

Method 3c overcomes all of the problems of methods 3a and 3b, but it introduces high compute, memory, and storage costs associated with the production and manipulation of 5D data sets. (We were able to use this method because we restricted the gathers to be outputted either only in a relatively small area or on a relatively sparse grid.) More importantly, this method encounters the

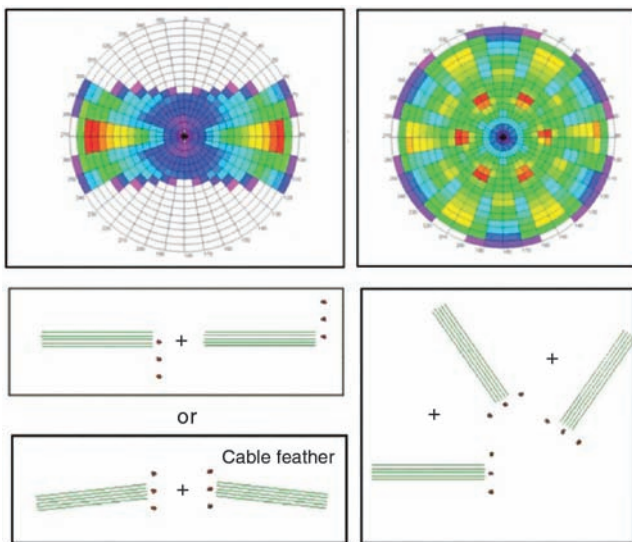


Figure 1. Rich-azimuth survey (rose diagram top right, source and streamer configuration lower right) has much more complete azimuth coverage compared to regular wide-azimuth surveys (rose diagram top left, source and streamer configurations mid and lower left). (Adapted from Howard, 2007).

new problem of contamination by edge diffractions in azimuth ranges not covered by the acquisition. These issues have limited its use.

Edge diffraction artifacts in RTM (or WEM) subsurface angle gathers are analogous to migration swings in Kirchhoff migrated gathers, but with very different appearance. In the Kirchhoff case, such swings occur near gaps or edges of the acquisition and can lead to erroneous residual moveout information that can cause velocity anomalies in tomography results. In the Kirchhoff case, this problem can be cured by muting each trace in the surface-offset CIGs based on its distance from the nearest input trace for its offset class. In the RTM case, such diffraction pattern results from the end-point diffractions generated by the edges and discontinuities of the recording geometry. These diffractions will mostly cancel out in the full stack, but they fail to cancel out for each azimuth-and-angle component of the image due to low (less than one) average fold of coverage contributing to any particular azimuth and angle. Unlike the Kirchhoff situation, it is difficult to remove these diffraction artifacts reliably from RTM angle gathers because these gathers are formed in the image domain and cannot be easily related back to recording geometry. Even for most current wide-azimuth surveys, the effective receiver pattern is not wide enough, or the shotpoints dense enough, to avoid these artifacts.

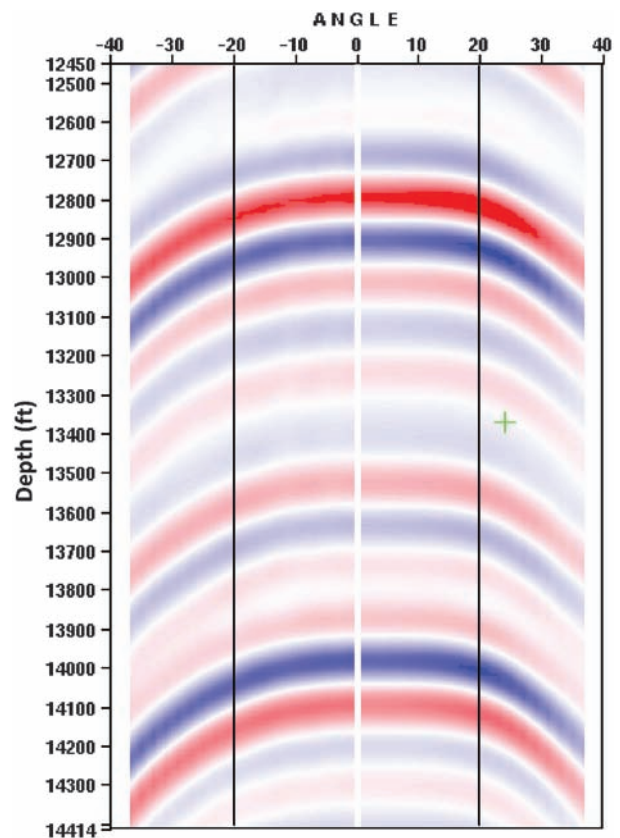


Figure 2. Two subsurface angle gathers from the same location, one generated with method 3a (using time shifts) and one with 3b (using subsurface inline offsets). They are displayed together in a "butterfly" manner to highlight their moveout difference. Only the absolute value of the angle label is meaningful. Result from method 3a is on the left half of the display. Angles are in degrees.

Figures 3 and 4 demonstrate the effect of these diffractions. Here, we use single-scattering modeling to generate synthetic shot records from a velocity model with a 3D salt body embedded in smooth sediment background (Figure 3a). Scatterers (including reflectors) in the model are the base of salt, three subsalt surfaces, and a grid of spherical scatterers (Figure 3b). In single-scattering forward modeling, a source-generated wavefield, the incident wave, is simulated first. This wavefield, multiplied with the reflectivity model, forms the source term for the reflected wavefield which is propagated separately. The synthetic seismic record is taken from the reflected wavefield only. As a result, the recorded data only contains reflections from the designated scatterers and are free of most types of multiples. This behavior fits our purpose, which is to study the primary reflections from the base salt and subsalt reflectors. The simulated acquisition geometry conforms to that of a typical Gulf of Mexico wide-azimuth survey, with inline offset ranging from 400 to 8000 m, and crossline offsets ranging from  $-4200$  to  $4200$  m. The synthetic data is migrated with the true velocity model, and the resultant 3D angle gathers are produced using method 3c.

Our 3D angle gathers are indexed by the subsurface angle of incidence and the azimuth of the reflection plane, defined as the azimuth of the horizontal line coplanar with the incident and reflected ray vectors (or slowness vectors, to be precise). This definition of azimuth ensures that subsurface reflection-plane azimuth and surface source-to-receiver azimuth are identical for

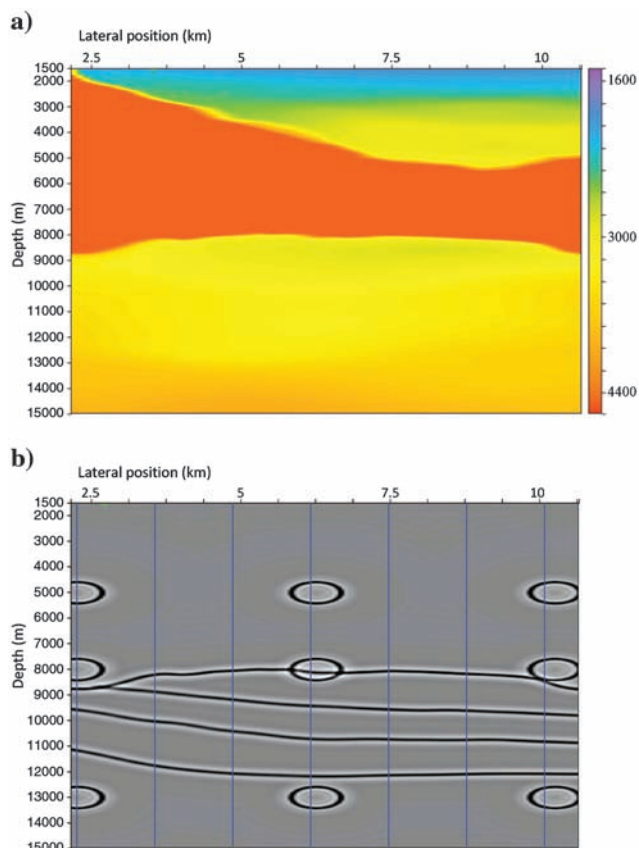


Figure 3. (a) Velocity model used in synthetic data generation and migration. (b) Reflectivity model used in single-scattering modeling. Blue lines mark locations of angle gathers displayed in the next figure.

constant velocity situations. From this point on in the text, wherever the context allows, we will for brevity refer to the angle of incidence as “angle” and the reflection-plane azimuth as “azimuth.” The conversion from extended images to 3D angle gathers is based on the description in Chapter 6 of Biondi (2006). The angle gathers from the synthetic test are shown in common-angle displays (Figure 4a) and common azimuth displays (Figure 4b and 4c). Evidently, the azimuth-and-angle ranges not illuminated by the acquisition contain diffraction patterns that are difficult to distinguish from azimuthally

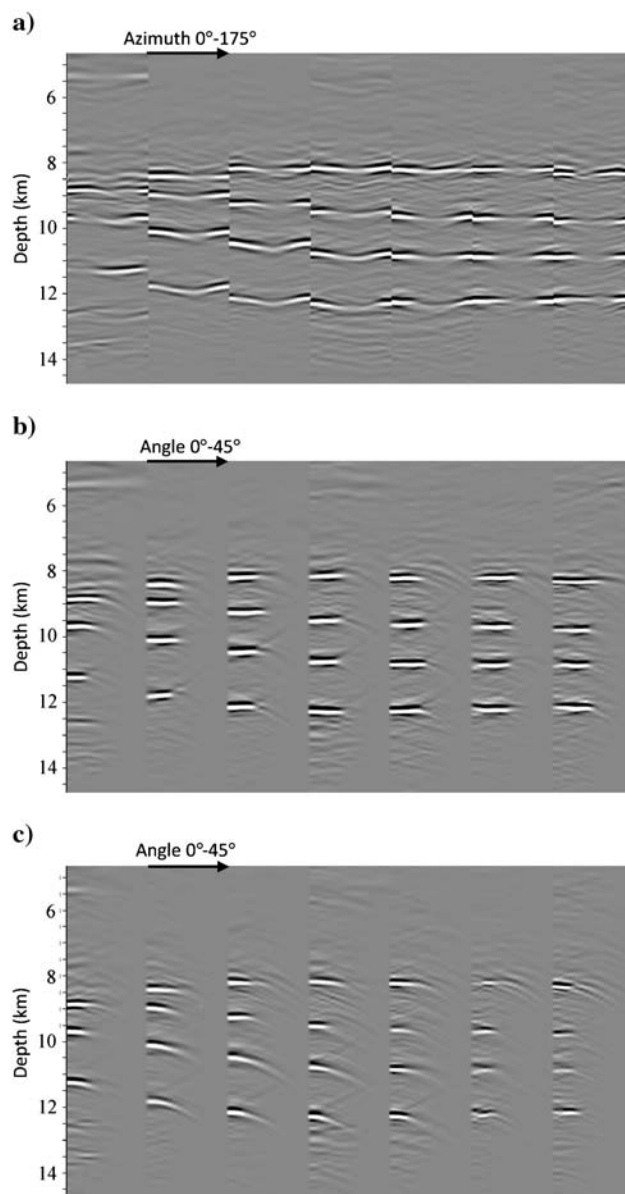


Figure 4. Three-dimensional angle gathers from locations marked in the Figure 3. (a) Common-angle display at angle =  $12^\circ$ . Each panel displays traces with azimuths from  $0^\circ$  to  $175^\circ$ . Note that there should be no residual moveout because the migration used correct velocity. (b) Common azimuth display at azimuth =  $0^\circ$ . Each panel displays traces with angle from  $0^\circ$  to  $45^\circ$ . These gathers appear essentially flat. (c) Common azimuth display at azimuth =  $70^\circ$ . These gathers contain diffraction artifacts and appear to have large residual moveout.

variable residual moveout, of which there should be none in this case. Velocity updates based on these gathers will likely contain large systematic error.

Rich-azimuth acquisition geometry is effectively full azimuth, minimizing the diffraction artifacts in the 3D angle gathers. For example, gathers generated from the Shenzi rich-azimuth data, shown in Figure 10, are largely free of harmful diffractions that can mislead velocity analysis. Some diffraction still exists due to irregularities of both surface geometry and subsurface illumination. These can be reduced by substacking the azimuth-and-angle gathers into fewer azimuth sectors, yielding more reliable residual moveout information.

**THE SHENZI MODEL BUILDING WORKFLOW**

The Shenzi rich-azimuth data was reprocessed starting in early 2009. Multi-azimuth 3D SRME was applied to the rich-azimuth data set as a whole. The model building workflow is conceptually outlined in Figure 5. Starting from a heavily smoothed, well-based, stratigraphic velocity model, parallel tomography workflows were carried out under vertical transverse isotropy (VTI) and TTI assumptions over two iterations to compare their effectiveness. For TTI models, we set the local axis of rotational symmetry to be perpendicular to the bedding planes. The results showed that the TTI approximation provides a better solution. Compared with the VTI result, the TTI migrated gathers were as flat or flatter, and the estimated model parameters were both smoother and more structurally conforming.

Figure 6 compares Thomsen anisotropy parameter epsilon from our VTI tomography with that from our TTI tomography. The VTI model contains low epsilon anomalies associated with regions with steep dips, which in a depth slice are regions with high-spatial frequency. These low epsilon anomalies, visible as blue to purple blobs in the figure, are an indication that the VTI assumption is a poor fit to data in that region. The anomalies are greatly reduced in the TTI model. Figure 7 shows a comparison of the V0 (P-wave velocity along local symmetry axis of VTI or TTI medium) model from a previous third party VTI processing effort with the V0 model from

our TTI tomography iterations. The VTI model contains velocity oscillations that do not correlate to well logs or structure.

Compared with a VTI image from previous processing, the new TTI model also greatly improved the top and base salt depth ties at numerous wells, including places where the salt exhibits complex 3D geometry and where the tie improvement is more than a mere vertical change in depthing (Figure 8). The improvements were evident even after just the first pass of salt picking.

Encouraged by these improvements, we decided to produce an intermediate product by combining the new TTI sediment background model with the old salt geometry model from the prior VTI processing. We vertically mapped the old VTI salt geometry model to time using the old VTI model, and back to depth using the new TTI sediment model. The resultant TTI RTM image proved to be a great improvement over the old VTI image in many places.

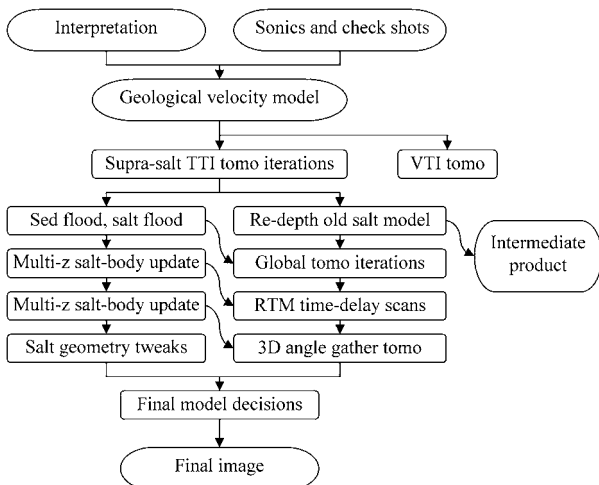


Figure 5. Conceptual outline of velocity model building workflow. Global tomography refers to updates which change velocity both above and below salt bodies, using gathers from migrations with preliminary salt models.

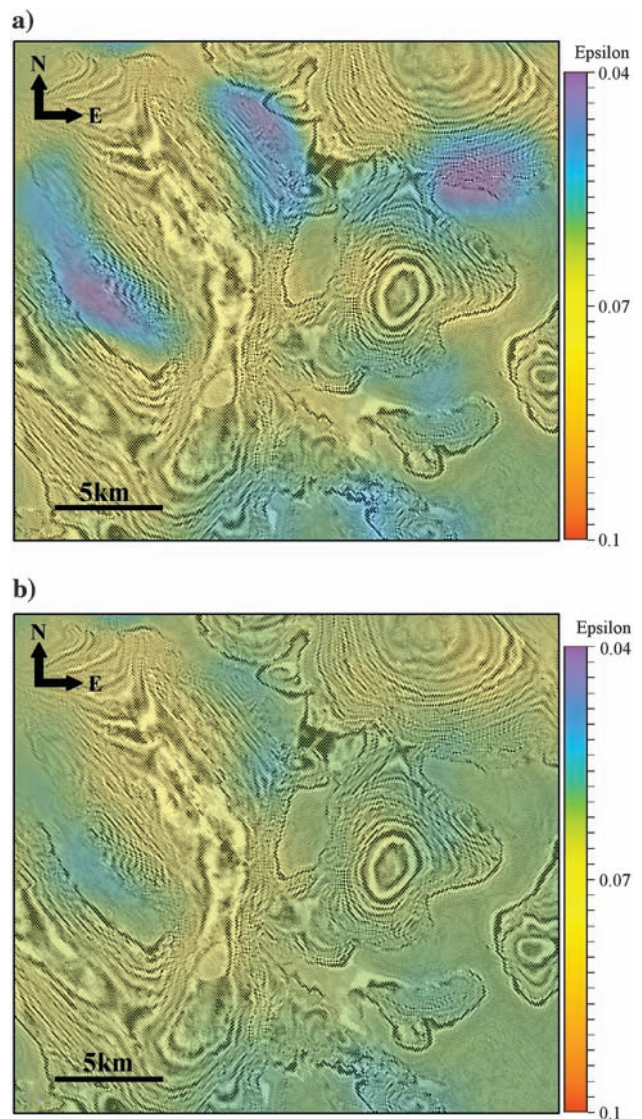


Figure 6. Depth slice displays of (a) VTI and (b) TTI tomographic inversion results for the epsilon parameter. Notice the presence of low epsilon anomalies along steeper basin flanks in the VTI result and the much smoother epsilon solution in the TTI result. The same inversion parameters were used in both runs.

This method of producing intermediate products made it possible to deliver an improved image to the end user even when we were still picking the first top of salt. We believe this method can be very useful in similar reprocessing projects involving long salt-model building cycle times, either to produce intermediate images for interpretation or to produce quality control (QC) images for evaluating suprasalt tomography.

We made further improvements to the image through multiple passes of salt geometry adjustments and iterations of tomographic update of the sediment velocity. The salt interpretation work employed a hybrid method combining picking on 2D sections with 3D solid model construction and manipulation, a multi-*z* approach that allowed the picking of multiple levels of salt in each iteration of the migration-interpretation cycle. This approach facilitated building a detailed complete salt model early in the workflow. The approach was not strictly top down, in that concurrent adjustments to top and base of salt or shallow and deep salt bodies were carried out.

Parallel to the early iterations of salt model building, we carried out tomography steps utilizing Kirchhoff offset-vector-tile gathers, generated with salt bodies in the velocity model. The focus of this step was to improve the sediment velocity model near steep salt flanks and below salt overhangs. Global updates were made to the sediment background so that velocities both above and below salt bodies were changed. However, the velocity changes above salt thus obtained were sufficiently small that vertical redepthing was adequate to realign the salt geometry with the updated sediment background.

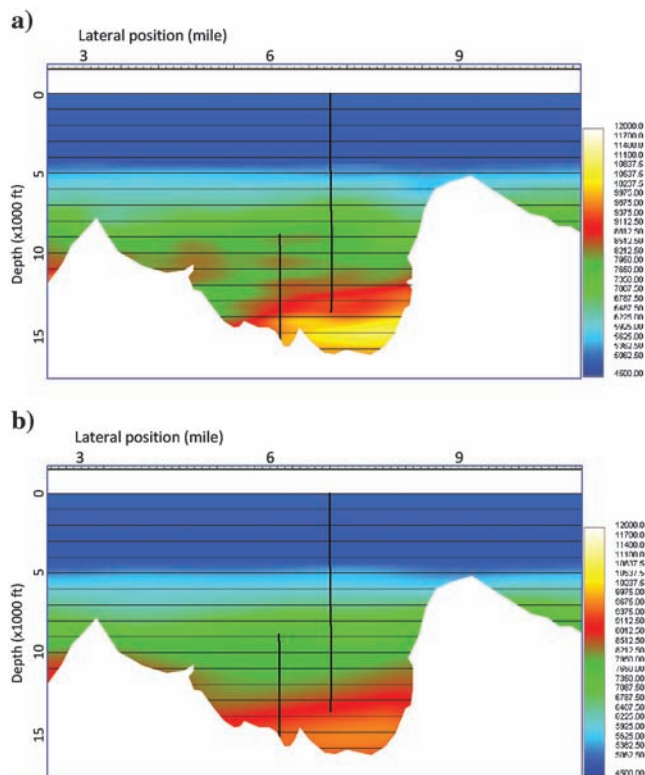


Figure 7. V0 displays of (a) previous VTI processing and (b) TTI reprocessing. The velocity oscillations in the VTI result do not match well logs. Black vertical lines are paths of deviated wells. White areas represent salt. Color scale is velocity in feet per second.

RTM-based subsalt updates followed the Kirchhoff-driven global tomography iterations. First, time-shift gathers (MacKay and Abma, 1992 and 1993; Wang et al., 2009) were used to detect any large-scale bias still present in the subsalt velocity. This method uses the time-shift extended imaging condition. But instead of converting the time-shift CIGs to angle gathers, this method directly examines the extended images by analyzing image amplitudes. The basic principle of this method is that, a bulk shift applied to seismic data alters the moveout curvature and hence the apparent moveout velocity. Under the *v*-of-*z* approximation, if the migration velocity is for instance too high, then a negative bulk shift of the appropriate amount will increase the apparent moveout velocity of the data so that the erroneous migration velocity will focus the time-shifted data. In other words, we can shift the data to improve the

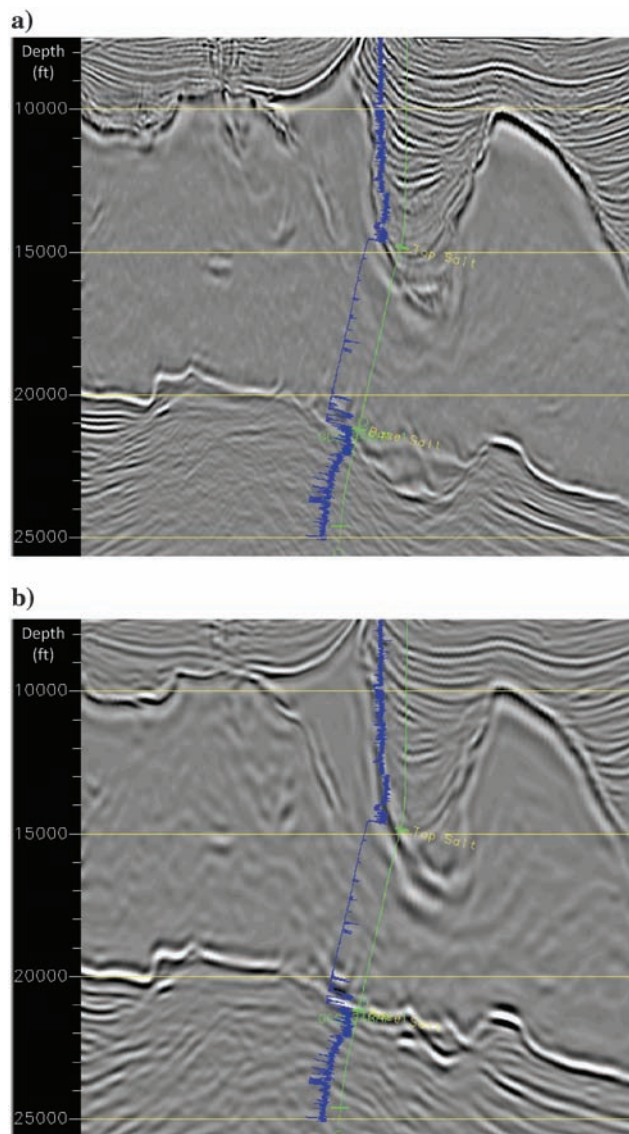


Figure 8. (a) Previous VTI image and (b) TTI reprocessing result. The TTI result better ties both the top and base salt and provides a more continuous image of the base salt. The TTI result is a lower-frequency QC image generated before subsalt updates and final salt geometry tweaks. (Horizontal axis is position along arbitrary line, and is unlabeled for confidentiality purposes.)

image focusing under any given velocity model. Conversely, the time shift that best focuses the image under a given velocity model can be used to compute an update to that model. Notably, the primary indication of improved focusing we have in this method is the image amplitude, which however is not always the highest for the “true” time shift because implied gather flatness is not the only contributor to stack amplitude. For instance, a syncline’s image amplitude can increase when it is undermigrated because undermigration shrinks the image of synclines, “concentrating” the amplitudes, and the converse is true for an anticline. In general, this method is best suited to identify velocity bias on a large length scale.

We generated time-shifted images from RTM with the shifts ranging from  $-1.2$  to  $1.2$  s at 30-ms steps. Spatially, these images are sampled the same as the regular stack image from the RTM. We then vertically redepthed each time-shifted image to the zero-time-shift depth (Figure 9a), using the local reflector dip and assuming  $5^\circ$  incidence angle. (Depth shift is equal to time-shift times half local velocity divided by the cosines of the dip angle and the incidence angle.) The energy envelope was computed for each trace to form pseudosemblance (Figure 9b). In Figure 9, the time-shifted images

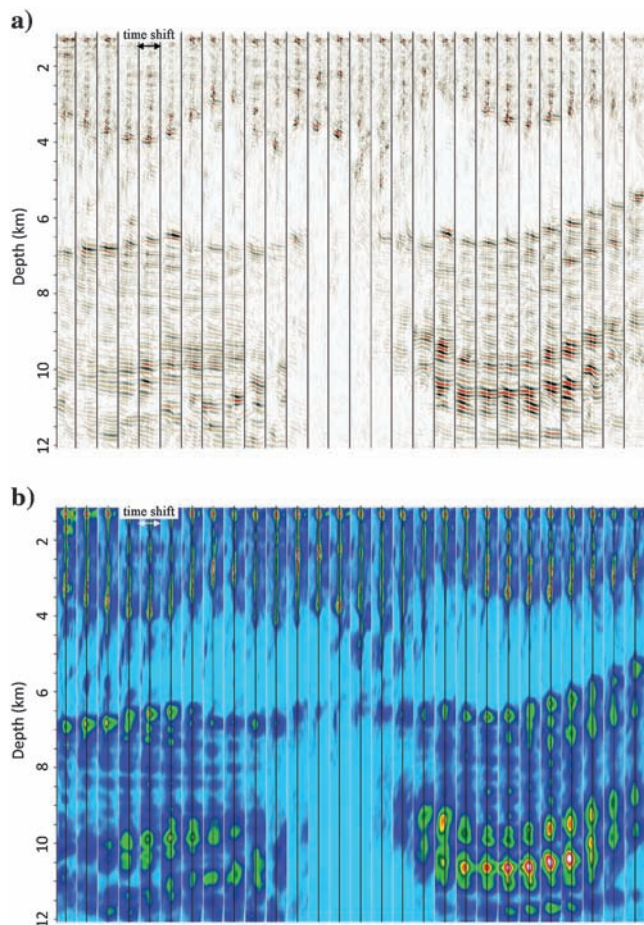


Figure 9. (a) RTM time-shift gathers and (b) pseudosemblance panels from select location across an inline. Each panel contains traces with time shifts ranging from  $-1.2$  to  $1.2$  s. These gathers are from locations 1 km apart. In (a), white vertical lines mark the zero time shifts for each panel, while in (b), black vertical lines mark the same.

are sorted into CIGs. After analyzing these time-delay gathers, we concluded that there was no significant large-scale subsalt velocity error left at this stage of model building and that remaining velocity errors should be addressed with a subsalt tomography based on RTM angle gathers. As a result, no attempt was made to pick time shifts or to compute velocity updates from time shifts.

So while final tweaks were being made to the salt geometry in localized regions to test different treatments for salt inclusions and for areas of uncertainty, we carried out a final pass of subsalt velocity update using RTM 3D angle gathers.

### 3D ANGLE GATHER FORMATION

We formed subsurface vector offset gathers from RTM and converted these gathers to 3D angle gathers postmigration (method 3c). Because we set the TTI symmetry axis to be locally normal to the bedding planes, incident and reflected waves of specular reflections from sedimentary reflectors have the same phase velocities near the reflector. As a result, we can treat the incidence and reflection phase angles as equal, simplifying the angle conversion process.

A subsurface offset domain CIG can be decomposed into dip components, each of which corresponds to a particular angle and azimuth. This correspondence implies a reciprocal relation between subsurface offset and subsurface angle. Therefore, the smaller the offset range, the lower the angle resolution. Excessively low angle resolution leads to angle gathers that are effectively trace mixed, i.e., low pass filtered in the angle dimension. Such gathers have reduced apparent residual moveout and lack crucial velocity information. After testing, we concluded that a minimum of 1.2 km of subsurface offset range was required to resolve residual moveout in the target subsalt section at about 10-km depth. This range could be reduced for the shallow, and the sampling density of the offset dimensions could be reduced for the deep, but we chose to avoid the complexity of implementing irregular sampling. And because we planned to perform global updates using angle gathers, the offset gathers must be sampled densely enough for the shallow, with a range large enough to resolve the deep. In our case, for a relatively low maximum migration frequency, these requirements resulted in subsurface offset gathers with 41 inline-offset samples and 41 crossline offset samples. We reduced it to  $21 \times 41$  through antipodal identification on the offset plane, but this was still a very high fold for the migration to generate due to the large amount of memory required for storing these gathers.

As a result, these subsurface offset gathers can only be generated at sparse locations. We chose a grid of roughly  $300 \times 120$  m to output these gathers. Due to this sparse sampling, 5D slant-stack or 5D Fourier-domain methods could not be employed to convert these subsurface offset gathers to azimuth-and-angle gathers. We must convert each subsurface offset CIG individually, using local reflector dips picked from the stack volume (Fomel, 2004). Such a conversion scheme applies only to specular reflections; it is appropriate for our purpose, which is to obtain velocity information from specular reflections. Under this approximation, the angle mapping of energy associated with subsurface diffractors is inaccurate, but other strengths of RTM angle gathers, such as the ability to properly handle multipathing, are retained.

The angle and azimuth resolution of the conversion can be estimated by converting into different angle and azimuth samplings. It was sufficient for our purpose to simply ensure that the resultant gathers were not aliased in either domain. We used a sampling

interval of  $4^\circ$  for the subsurface azimuth, with the range being from  $0^\circ$  to  $176^\circ$ . (Azimuth is referenced to the local processing coordinate system from this point on in the text. In this system,  $0^\circ$  is east, and  $90^\circ$  is south.) This range only covering a half plane was a result of the antipodal identification used in the generation of subsurface offset gathers. A sampling interval of  $3^\circ$  was chosen for the incidence angle, with useful range subsalt being from  $3^\circ$  to  $36^\circ$ . The  $3^\circ$  minimum angle was due to the survey's average near offset being approximately 800 m and the maximum target depth for subsalt moveout analysis being 10 km.

Figure 10a displays a single such 3D angle gather, sorted so that traces with the same angle are grouped together. It is evident from this display that the data has relatively uniform azimuth coverage subsalt at  $15^\circ$  angle of incidence or below, while the coverage becomes notably uneven beyond  $18^\circ$ . It also suggests that, if we substack the 3D angle gathers into four azimuth sectors, we will have good coverage in each sector, so that the residual moveout measured in each sector will not be dominated by diffraction artifacts.

A transposed view of the same gather, sorted so that traces with the same azimuth are grouped together (Figure 10b), shows that

there is a small amount of azimuthally varying residual moveout at this location. The poorly illuminated azimuth subsalt is around  $18^\circ$ , which is a relatively well-illuminated azimuth at the water bottom level. This difference clearly demonstrates that subsalt reflection azimuth is often not aligned with surface azimuth, and that azimuth sectoring based on subsurface geometry is different from sectoring of input data by source-to-receiver azimuth. This difference also highlights the importance of the use of subsurface geometric attributes when forming CIGs.

Similar behavior was observed in broader views of the data. Figure 11 shows common-angle displays of regularly spaced subsets of gathers across an inline. It is again clear that azimuthal coverage subsalt becomes uneven at  $21^\circ$ . Led by such analysis, we chose to substack the 3D angle gathers into four azimuth sectors, centered at  $0^\circ$ ,  $45^\circ$ ,  $90^\circ$ , and  $135^\circ$ , respectively. (These values are referenced to our processing coordinate system described earlier.) The azimuth range for each sector extended  $22.5^\circ$  on either side of the center. Azimuths  $180^\circ$  apart were considered equivalent. The central azimuth of each sector was used as the nominal azimuth for that sector in the tomography. Using azimuth sectors was expected to reduce

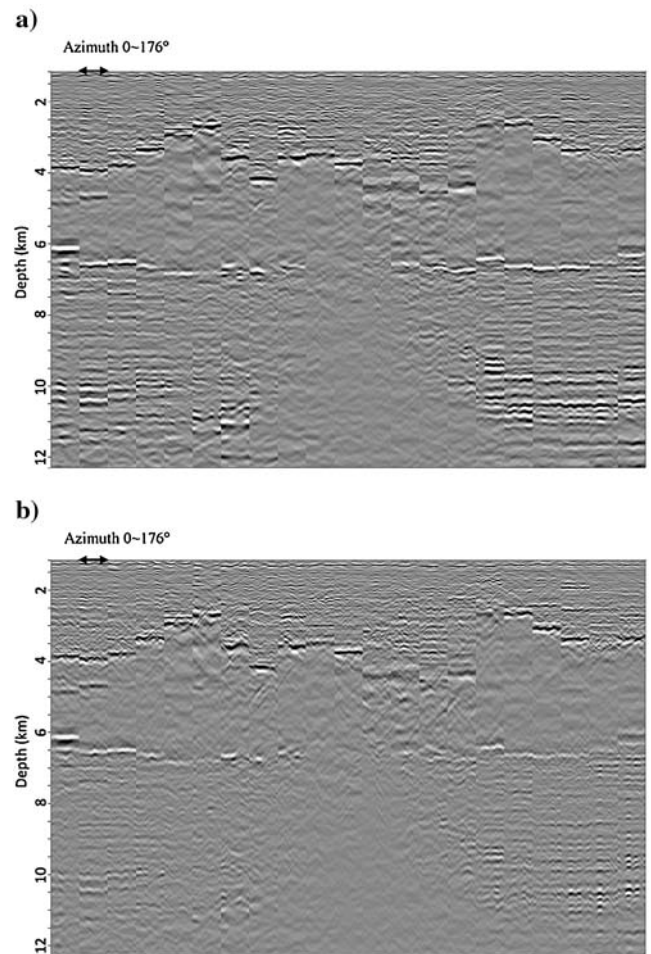


Figure 10. A single 3D angle gather: (a) Angle-azimuth order display. Numbers across the top are incidence angle for each panel, with azimuth ranging from  $0^\circ$  to  $176^\circ$  within each panel. (b) Azimuth-angle order displays. Numbers across the top are azimuth for each panel, with incidence angle ranging from  $3^\circ$  to  $36^\circ$  within each panel.

Figure 11. Common-angle displays of a regular subset of gathers along an inline, at incidence angle of (a)  $15^\circ$  and (b)  $21^\circ$ . Each panel contains traces with azimuths ranging from  $0^\circ$  to  $176^\circ$ . Notice the appearance of diffraction artifacts in the  $21^\circ$  section in b), as some azimuths are not illuminated at this relatively large angle. The gathers are from locations 1.4 km apart.

the accuracy of tomography, but this was a necessary compromise to avoid contamination from diffraction artifacts. Figure 12 displays such azimuth sectored angle gathers from select CDP locations across an inline. In this display, azimuthal and spatial variations in the residual moveout can be identified.

### MULTIAZIMUTH SUBSALT TOMOGRAPHY

The last step of processing applied to the angle gathers was an angle-and-depth domain mute to remove diffraction artifacts in the small angles up shallow and large angles down deep (Figure 13). For example, at 1200-m water bottom depth, an average near offset of 800 m yields a minimum angle of  $16^\circ$ . Similarly, with a straight

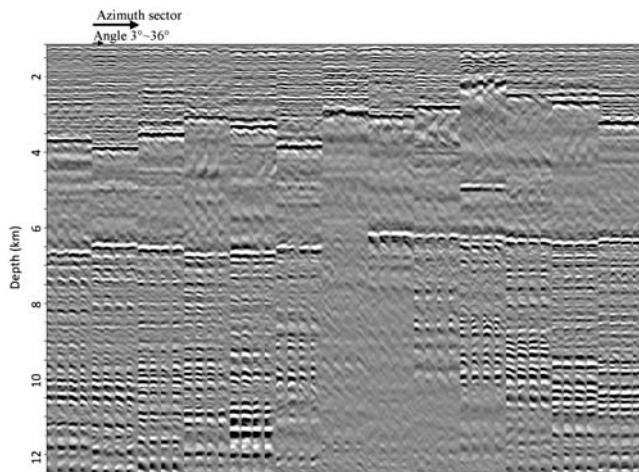


Figure 12. Three-dimensional angle gathers substacked into four azimuth sectors. A regular subset from a 2.1 km sampling interval is displayed. Each panel contains four subpanels, one for each azimuth sector. Each subpanel contains traces with angles ranging from  $3^\circ$  to  $36^\circ$ . Spatially and azimuthally variable residual moveout can be observed. Notice the velocity information in these gathers is more distinct than that in the time-shift gathers.

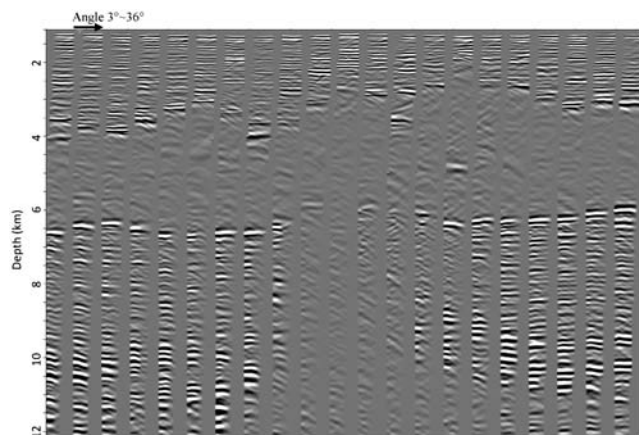


Figure 13. A regular subset of muted angle gathers from one azimuth sector along an inline. An inner mute is applied in the shallow section, to reflect the average near offset of  $\sim 800$  m. An outer mute is applied in the deep section, to reflect the lack of offsets beyond  $\sim 7.5$  m. The gathers are from locations 1.4 km apart.

ray assumption, a 7.6-km maximum offset yields a  $\sim 17^\circ$  maximum angle at 12-km depth. The range of well-covered angles is depth variable, and beyond this range, the angle gather traces are dominated by diffraction artifacts.

Each sector of angle gathers was automatically picked to obtain residual moveout measures. In Figure 14, we display the moveout curvatures, in color and overlaid with the underlying seismic sections, from two of the four azimuth sectors. Clearly visible are both a general similarity and localized differences between the two moveout curvature sections. It is important to capture such azimuthal variations in the residual moveout to enable tomography to better identify localized velocity errors. The four sectors of residual moveout measures were jointly inverted in a ray-based TTI tomographic inversion to obtain a velocity update. The tomography was allowed to update the model everywhere except for within the salt and water regions.

Tomography cannot resolve the ambiguity between  $V_0$  and  $\delta$ , and a priori constraints must be applied to resolve the ambiguity. Various constraints were tested, including 1) keeping  $\delta$  constant or 2) keeping  $\delta$  within a given range of values while maintaining

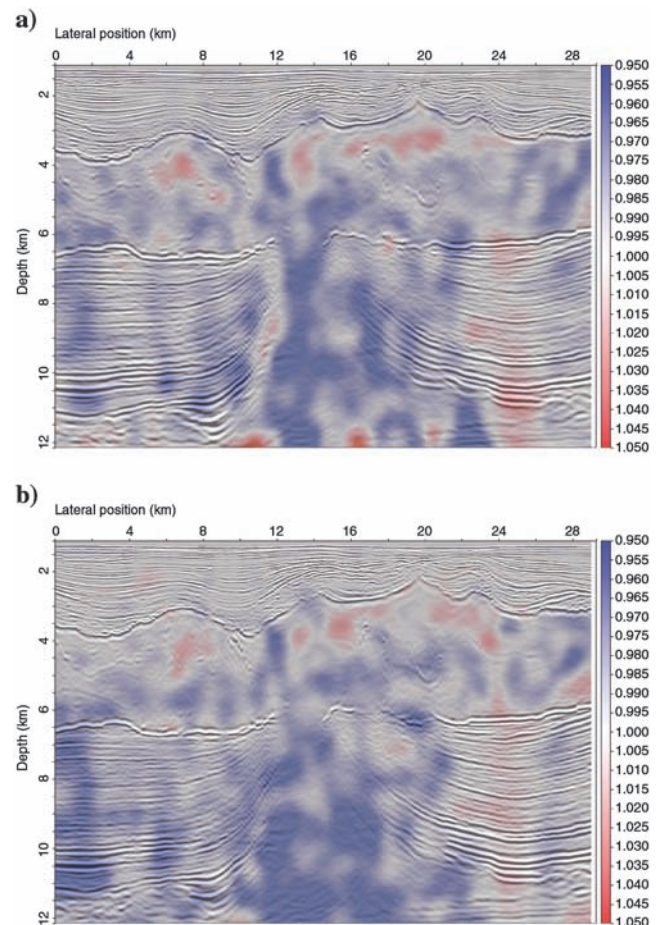


Figure 14. Residual moveout curvature measured from the (a)  $0^\circ$  and (b)  $90^\circ$  azimuth sectors, displayed here in color, overlaid with seismic in gray scale. Moveout is parameterized as true velocity over migration velocity, in the rms sense. Note the large scale similarity and local differences between the moveout measures from the two azimuths.

subsalt well-seismic ties. Epsilon and TI symmetry axis inclination and orientation were treated as constants in the tomography runs.

We used TTI RTM runs to evaluate the multiple versions of updated subsalt velocities and compare them with the preupdate image. Of the different updates, the simultaneous V0-and-delta update result was judged the best. Compared to the preupdate image,

the update result showed widespread improvements in the subsalt image. In the example shown in Figure 15, the updated model improved the imaging of the lower sections of the subsalt minibasin, increased stack amplitude and coherency, and reduced structural undulations in the reflectors, thereby simplifying the structural picture. Figures 16, 17, 18, and 19 show examples where the update

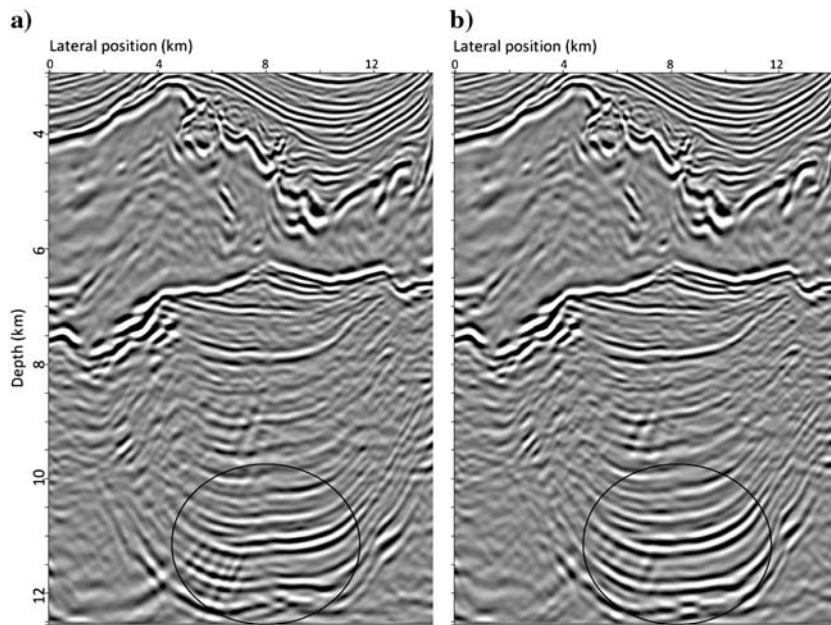


Figure 15. (a) Before and (b) after subsalt velocity update. Note the simplified structural style of the subsalt basin.

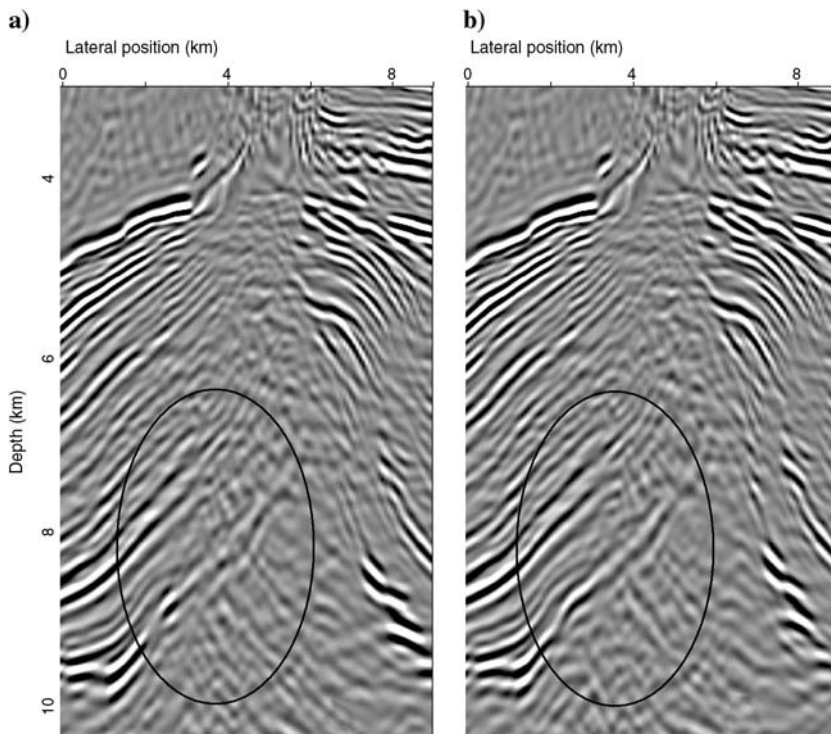


Figure 16. (a) Before and (b) after subsalt velocity update.

improved the event continuity and stack amplitudes of the subsalt section.

### FINAL STACK IMAGE OPTIMIZATION USING 3D ANGLE GATHERS

After finalizing all aspects of the velocity model, we generated 3D angle gathers from the final RTM for the purpose of creating a

residual moveout corrected stack image. The gathers must be sampled on a grid as dense as the stack image. Such dense sampling enabled the use of 5D slant stack for subsurface offset-to-angle mapping. We chose a 160 km<sup>2</sup> area to output densely sampled 3D angle gathers. The subsurface offset-vector sampling and the azimuth-and-angle samplings after the conversion were similar to those used during the subsalt velocity update. Due to the dense

Figure 17. (a) Before and (b) after subsalt velocity update.

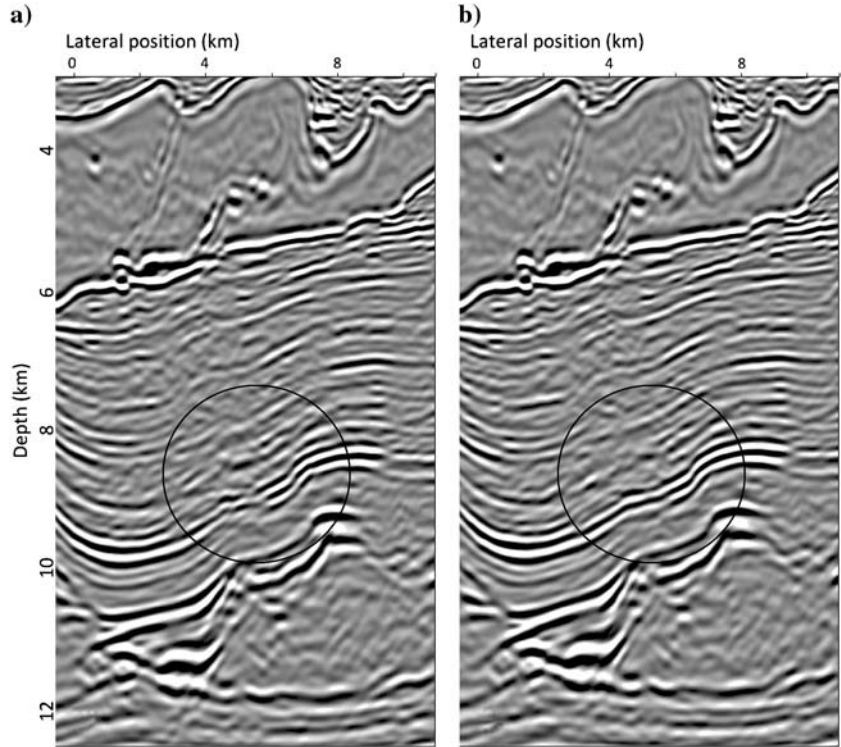
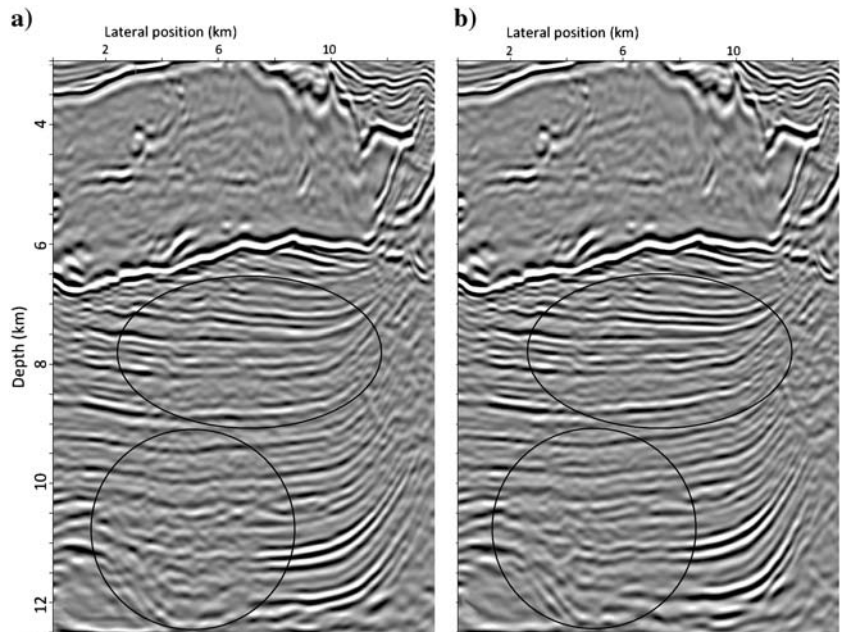


Figure 18. (a) Before and (b) after subsalt velocity update.



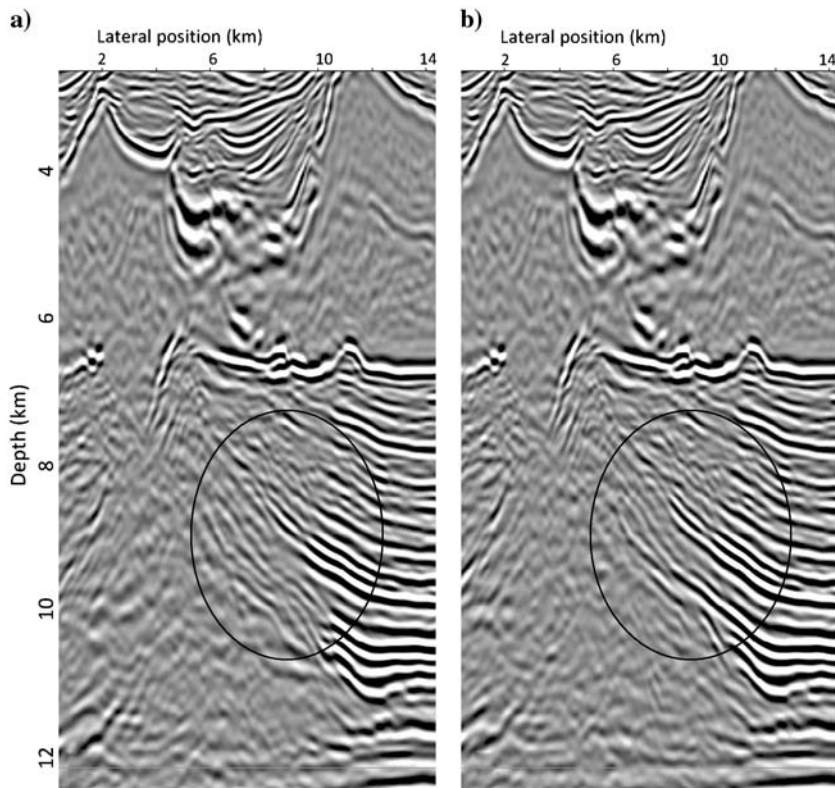


Figure 19. (a) Before and (b) after subsalt velocity update.

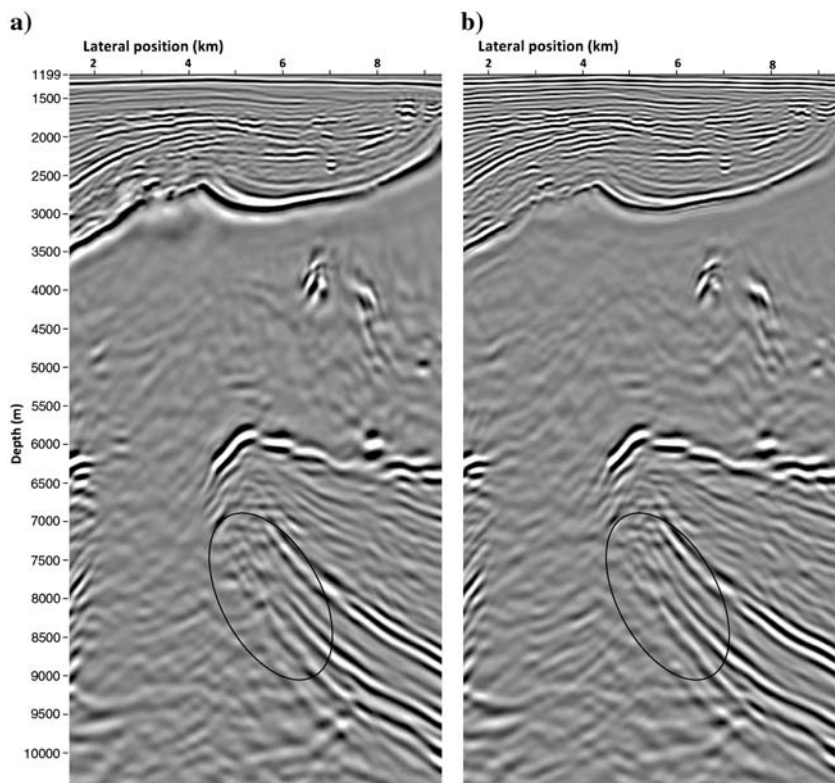


Figure 20. (a) Normal image from RTM. (b) Residual moveout corrected angle stack. Difference in the suprasalt section is due to the angle limit in the angle stack.

Figure 21. Residual moveout corrected stacks of the (a) 0° and (b) 60° azimuth sectors.

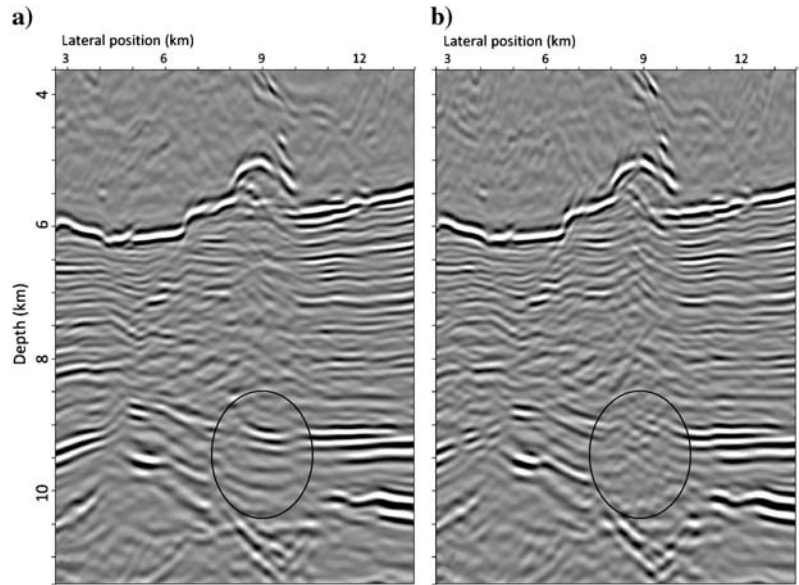


Figure 22. Azimuthally substacked angle gathers from the (a) 60° and (b) 0° azimuth sectors. Note the energy present in the 0° sector on far-angle range in the poorly imaged area. Maximum angle of incidence displayed is 27°. These gathers are from locations 1.4 km apart.

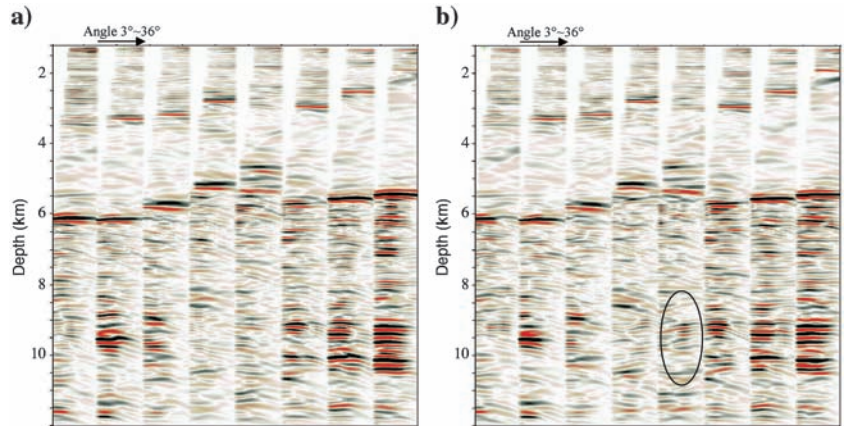
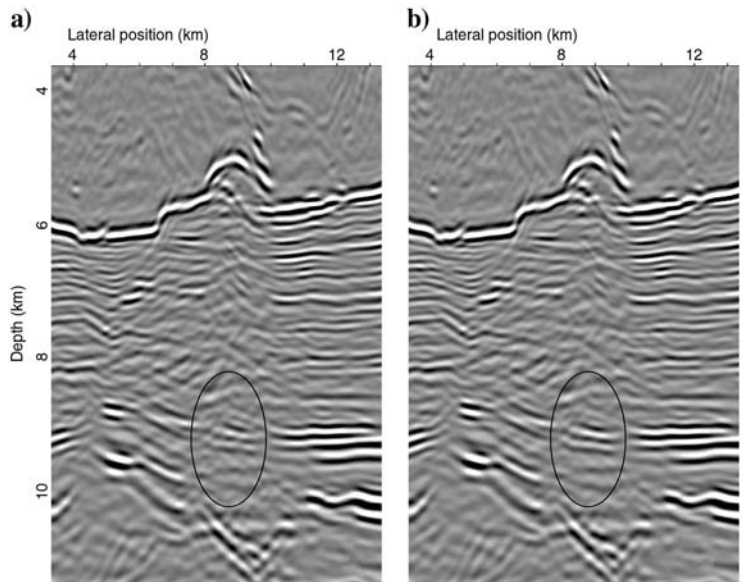


Figure 23. (a) Straight sum of the three azimuthal sectors. (b) Optimized stack of the azimuthal sectors.



spatial sampling, we were able to use the 5D fast Fourier transform based method for the angle conversion in this case. Residual moveout correction was performed separately for each azimuth sector as before, but we determined that the use of three sectors produced better final stack. The azimuth sectors are centered at 0°, 60°, and 120° in the processing coordinate system. The sum of the three azimuth sectors after separate residual moveout correction yielded an improved image in some areas compared to the normal stack image from the RTM (Figure 20).

We also noticed that in some areas, particularly places where the uncertainty in the salt geometry is large, the different azimuth sectors had very different subsalt illumination gaps. In Figure 21, we show an example where, under a region of complicated base salt, the image in the 60° azimuth sector has an illumination-gap-induced migration swing, whereas the 0° azimuth sector is able to image much of the structure. Figure 22 shows that the image in the 0° sector is formed by energy associated with relatively large angle of incidence, i.e., raypaths which undershoot the base salt complexity. An automatic selective stacking process was adopted to exclude the illumination-gap-induced migration swings from the final stack, producing an optimized stack image that is superior to the straight sum of the three azimuth sectors (Figure 23).

### CONCLUSION

We demonstrated that RTM 3D subsurface angle gathers can be used in subsalt tomographic velocity model update to significantly improve subsalt image. We showed that care must be taken when using angle gathers for velocity update. Two-dimensional angle gathers from time-shift or subsurface offset methods are inaccurate. And 3D angle gathers can contain strong artifacts when the input data has insufficient azimuth coverage. We showed that the rich-azimuth acquisition method, which produces nearly full azimuthal coverage, supports the generation of largely artifact-free 3D angle gathers. To further remove artifacts, we substacked the 3D angle gathers azimuthally into a small number of azimuth sectors for residual moveout analysis and multiazimuth subsalt tomography. The updated velocities led to widespread improvements in subsalt imaging, resulting in enhanced interpretability of the data. Three-dimensional angle gathers calculated during the final migration were also successfully used through gather flattening and selective stacking to produce an optimized final stack.

While 3D angle-gather generation techniques have been known for several years, few successful cases of their use for subsalt model updates have been reported. As our work demonstrates, with a full understanding of the characteristics and limitations of the various types of angle gathers, and using appropriate procedures for conditioning them, one can obtain reliable subsalt velocity updates from these gathers.

### ACKNOWLEDGMENTS

We thank BHP Billiton and the Shenzi Partnership for permission to publish this work. We thank the model building teams at BHPB, the Partnership companies, and GXT for their support during this work.

### REFERENCES

- Biondi, B., 2006, 3D seismic imaging: Investigations in geophysics, No. 4: SEG.
- Biondi, B., and T. Tisserant, 2004, 3D angle-domain common-image gathers for migration velocity analysis: *Geophysical Prospecting*, **52**, no. 6, 575–591, doi: [10.1111/gpr.2004.52.issue-6](https://doi.org/10.1111/gpr.2004.52.issue-6).
- de Bruin, C. G. M., C. P. A. Wapenaar, and A. J. Berkhout, 1990, Angle-dependent reflectivity by means of prestack migration: *Geophysics*, **55**, 1223–1234, doi: [10.1190/1.1442938](https://doi.org/10.1190/1.1442938).
- Fomel, S., 2004, Theory of 3-D angle gathers in wave-equation imaging: 74th Annual International Meeting, SEG, Expanded Abstracts, 1053–1056.
- Howard, M., 2007, Marine seismic surveys with enhanced azimuth coverage: Lessons in survey design and acquisition: *The Leading Edge*, **26**, no. 4, 480–493, doi: [10.1190/1.2723212](https://doi.org/10.1190/1.2723212).
- Macesanu, C., J. H. Higginbotham, and M. P. Brown, 2010, Angle decomposition for one-way wave equation migration: 80th Annual International Meeting, SEG, Expanded Abstracts, 3242–3245.
- MacKay, S., and R. Abma, 1992, Imaging and velocity estimation with depth-focusing analysis: *Geophysics*, **57**, 1608–1622, doi: [10.1190/1.1443228](https://doi.org/10.1190/1.1443228).
- MacKay, S., and R. Abma, 1993, Depth-focusing analysis using a wave-front-curvature criterion: *Geophysics*, **58**, 1148–1156, doi: [10.1190/1.1443498](https://doi.org/10.1190/1.1443498).
- Nolan, C., and W. W. Symes, 1996, Imaging in complex velocities with general acquisition geometry: Annual Report: The Rice Inversion Project, Rice University.
- Rickett, J. E., and P. C. Sava, 2002, Offset and angle-domain common image-point gathers for shot-profile migration: *Geophysics*, **67**, 883–889, doi: [10.1190/1.1484531](https://doi.org/10.1190/1.1484531).
- Sava, P., and S. Fomel, 2006, Time-shift imaging condition in seismic migration: *Geophysics*, **71**, no. 6, S209–S217, doi: [10.1190/1.2338824](https://doi.org/10.1190/1.2338824).
- Sava, P., and I. Vasconcelos, 2011, Extended imaging conditions for wave-equation migration: *Geophysical Prospecting*, **59**, 35–55, doi: [10.1111/gpr.2010.59.issue-1](https://doi.org/10.1111/gpr.2010.59.issue-1).
- Soubaras, R., 2003, Angle gathers for shot-record migration by local harmonic decomposition: 73rd Annual International Meeting, SEG, Expanded Abstracts, 889–892.
- Wang, B., C. Mason, M. Guo, K. Yoon, J. Cai, and Z. Li, 2009, Subsalt velocity update and composite imaging using reverse-time-migration based delayed-imaging-time scan: *Geophysics*, **74**, no. 4, E159–E166, doi: [10.1190/1.3131382](https://doi.org/10.1190/1.3131382).
- Wu, R. S., M. Luo, S. Chen, and X. Xie, 2004, Acquisition aperture correction in angle-domain and true-amplitude imaging for wave equation migration: 74th Annual International Meeting, SEG, Expanded Abstracts, 937–940.
- Xu, S., H. Chauris, G. Lambare, and M. Noble, 2001, Common angle image gather — A strategy for imaging complex media: *Geophysics*, **66**, 1877–1894, doi: [10.1190/1.1487131](https://doi.org/10.1190/1.1487131).
- Xu, S., Y. Zhang, and B. Tang, 2010, 3D common image gathers from reverse time migration: 80th Annual International Meeting, SEG, Expanded Abstracts, 3257–3262.
- Yoon, K., K. J. Marfurt, and W. Starr, 2004, Challenges in reverse-time migration: 74th Annual International Meeting, SEG, Expanded Abstracts, 1057–1060.